A Note on Curvelets and Multiscale Directional Transforms (Signal analysis and time-frequency analysis)

AUTHOR(S):

Fujinoki, Kensuke

CITATION:

Fujinoki, Kensuke. A Note on Curvelets and Multiscale Directional Transforms (Signal analysis and time-frequency analysis). 数理解析研究所講究録 2019, 2102: 8-31

ISSUE DATE:

2019-02

URL:

http://hdl.handle.net/2433/251829

A Note on Curvelets and Multiscale Directional Transforms

Kensuke Fujinoki
Department of Mathematical Sciences, Tokai University

Abstract

We present a brief review on curvelets while describing their related topics in efficient representations for a multivariate function. Starting from the approximation theory by a frame in a Hilbert space, we attempt to construct a family of curvelets and to show that it forms a tight frame. A short introduction of other multiscale multidirectional methods, namely, ridgelets, shearlets and contourlets, is also presented.

1 Efficient Representations for an Image

In neuropsychological studies, the importance of directional sensitivity in the efficient processing of natural images by the human brain has been a major finding, as in a seminal study by Field and Olshausen in *Nature* [41]. Research on efficient representations of images has also been conducted in both the fields of applied mathematics and electrical engineering, especially computational harmonic analysis and signal processing.

As a typical example, wavelet systems are widely used for a range of image processing tasks, as well as in other scientific fields. For additional details on wavelets and their applications, see [51, 38]. Despite their popularity, however, wavelet-based approaches are not very effective when dealing with multivariate data, i.e., an image in $\mathbb{R}^2$, that contains singularities along curved edges due to their support (see Figure 1).

This problem had been recognized in the early filter bank literature, and, in order to tackle this obstacle, a number of directional wavelet-based approaches have been proposed, including the steerable pyramid (Simoncelli et al. [46]), directional filter banks (Bamberger and Smith [3]), nonseparable multidimensional wavelets (Kovačević and Vetterli [30]), 2D directional wavelets (Antoine et al. [1]), and complex wavelets (Kingsbury [29]).

However, even though they frequently outperform standard wavelets in some applications, none of these methods provides optimally sparse approximations of multivariate data that have anisotropic features. The fundamental reason for this failure is that these approaches are not truly multidimensional extensions of the wavelet approach.

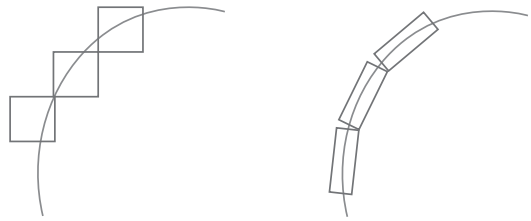

Figure 1: Representations of a curved edge by a wavelet (left) and an ideal method (right).

A breakthrough occurred with the introduction of curvelets by Candès and Donoho in 2004 [10]. This approach has brought about significant developments in this field and has established a new kind of multiscale method, called *geometric multiscale analysis*. The decade from 2000 to 2010 saw developments in geometric multiscale analysis, as well as several other developments in directional wavelets in multidimensions, which are referred to as *X–lets*, including bandelets [42, 43], brushlets [40], contourlets [21], curvelets [10, 11, 12], directionlets [54], framelets [20], grouplets [39], ridgelets [7, 8], shearlets [31], and wedgelets [22]. We will not, however, introduce all types of X–lets here, but for a brief introduction of X–lets, please see [37].

Contents

In this paper, we focus on curvelets and their related topics. There are two generations of curvelets. The first-generation curvelets is developed in a continuous domain with multiscale filtering and a block ridgelet transform on each bandpass image [9], whereas the second-generation curvelets are constructed by direct 2D frequency partitioning based on polar coordinates without the ridgelet transform [10]. Although a well-written review paper has been published by Ma and Plonka [37], they concentrated primarily on second-generation curvelets. This paper is intended to include a much wider range of topics regarding all generations of curvelets.

This paper is organized as follows. In Sections 2 and 3, we introduce an approximation theory and a frame theory, respectively, because curvelets form a tight frame. Section 4 introduces ridgelets, which are used in the construction of first-generation curvelets. Sections 5 and 6 introduce first- and second-generation curvelets, respectively, and their applications. Finally, we mention other multidirectional wavelets, namely, shearlets and contourlets, in Section 7.

2 Approximation Theory

We begin with a classical approximation theory for a function in a Hilbert space. In particular, we consider $L^2(\mathbb{R}^2)$ throughout this paper. Let $\{\phi_m\}_{m=1}^{\infty}$ be an orthonormal basis of $L^2(\mathbb{R}^2)$. For all $f \in L^2(\mathbb{R}^2)$, we have the expansion

$$f = \sum_{m=1}^{\infty} \langle f, \phi_m \rangle \, \phi_m, \tag{1}$$

where $\langle f, g \rangle = \int_{\mathbb{R}^2} f(x)\overline{g(x)}\, dx$ is an inner product, and $\bar{z}$ is the complex conjugate of z. The norm is defined as $\|f\| = \langle f, f \rangle^{1/2}$. This expansion gives an exact reconstruction of f in the L^2 sense, but, for some computations, it is convenient to consider a linear approximation with the finite sum:

$$f_M = \sum_{m=1}^{M} \langle f, \phi_m \rangle \, \phi_m,$$

which is referred to as the M-term linear approximation of f. In general, this expansion produces an approximation error $\|f - f_M\|^2$, which depends on M. Since $\{\phi_m\}_{m=1}^{\infty}$ is an orthonormal basis of $L^2(\mathbb{R}^2)$, the resulting approximation error $\|f - f_M\|^2$ is written as the sum of the remaining coefficients:

$$\|f - f_M\|^2 = \sum_{m=M+1}^{\infty} |\langle f, \phi_m \rangle \, \phi_m|^2.$$

While the quality of f_M depends on properties of the basis function $\{\phi_m\}_{m=1}^{M}$, the best approximation that minimizes $\|f - f_M\|^2$ is obtained by selecting the M largest terms of the coefficients $|\langle f, \phi_m \rangle|$ by a threshold $T_M > 0$, which is referred to as the nonlinear approximation of f:

$$f_M = \sum_{m \in I_M} \langle f, \phi_m \rangle \, \phi_m,$$

where $I_M = \{m \in \mathbb{N} : |\langle f, \phi_m \rangle| > T_M\}$. The approximation error immediately follows from $\|f - f_M\|^2 = \sum_{m \notin I_M} \langle f, \phi_m \rangle \, \phi_m$. For some applications, such as image compression, we want to have a sparse representation of f. In general, if an image f is uniformly regular, i.e., $f \in C^{\alpha}$, and if a wavelet ψ has $p > \alpha$ vanishing moments, then there exists a constant $C > 0$ such that

$$\|f - f_M\|^2 \leq C M^{-\alpha}, \qquad M \to \infty,$$

where we assumed that f_M is obtained by the best M wavelet terms. This is a fairly good approximation rate and is the reason why a wavelet system is known to provide an

optimally sparse approximation of a function, as compared with traditional Fourier-based methods.

However, if an image has discontinuities along outside curves, the best M-term wavelet approximation fails as

$$\|f - f_M\|^2 \leq CM^{-1}, \qquad M \to \infty.$$

However, a wavelet series is better than the Fourier series because the Fourier approximation achieves only $\|f - f_M\|^2 \leq CM^{-1/2}$ as $M \to \infty$. When we consider an adaptive approach that selects terms from an overcomplete correction of basis functions, the best approximation rate is known to be

$$\|f - f_M\|^2 \leq CM^{-2}, \qquad M \to \infty$$

for an image f that has curve singularities (see [9]).

The Fourier and wavelet approximations both use fixed transforms and are thus nonadaptive approaches. Curvelets are also nonadaptive, but, surprisingly, they achieve

$$\|f - f_M\|^2 \leq CM^{-2} (\log M)^3, \qquad M \to \infty.$$

This is optimal in the sense that no other nonadaptive representation can yield a smaller asymptotic error with the same number of terms. In fact, curvelets also essentially provide optimally sparse representations of Fourier integral operators [13, 14].

On the other hand, the bandlet method, as proposed by Pennec and Mallat [42, 43], is a powerful tool for representing smooth edges. The bandlet system achieves an optimal approximation estimate for an image that contains curved edges beyond C^2, namely, C^κ, $\kappa > 2$:

$$\|f - f_M\|^2 \leq CM^{-\kappa}, \qquad M \to \infty.$$

However, this method requires an extra edge detection stage, followed by an adaptive representation, and therefore is categorized as an adaptive approach.

3 Frame Theory

A curvelet system is a tight frame of $L^2(\mathbb{R}^2)$. Frame theory was first introduced in the mid-20th century by Duffin and Schaeffer [24] and was then revived by Daubechies in the 1990s [19]. A sequence $\{\varphi_m\}_{m=1}^{\infty}$ in $L^2(\mathbb{R}^2)$ is called a frame for $L^2(\mathbb{R}^2)$ if, for all $f \in L^2(\mathbb{R}^2)$, there exist two constants $0 < A \leq B < \infty$ such that

$$A\|f\|^2 \leq \sum_{m=1}^{\infty} |\langle f, \varphi_m \rangle|^2 \leq B\|f\|^2,$$

where A and B are called frame bounds.

In the case of $A = B$, a frame $\{\varphi_m\}_{m=1}^{\infty}$ is called a *tight frame*, which satisfies, for all $f \in L^2(\mathbb{R}^2)$,

$$\sum_{m=1}^{\infty} |\langle f, \varphi_m \rangle|^2 = A\|f\|^2.$$

This implies that we have an expansion

$$f = \frac{1}{A} \sum_{m=1}^{\infty} \langle f, \varphi_m \rangle \, \varphi_m, \tag{2}$$

which is similar to the orthonormal expansion (1). Thus, the tight frame has a remarkable property that it can recover f from the coefficients $\langle f, \varphi_m \rangle$ in the L^2 sense, and thus (2) is referred to as the perfect reconstruction property of a frame.

A tight frame with the frame bounds $A = 1$ is also called a *Parseval frame*. Obviously, we have

$$f = \sum_{m=1}^{\infty} \langle f, \varphi_m \rangle \, \varphi_m, \tag{3}$$

and

$$\sum_{m=1}^{\infty} |\langle f, \varphi_m \rangle|^2 = \|f\|^2.$$

As shown above, a tight/Parseval frame is very similar to an orthogonal/orthonormal basis. In fact, if a Parseval frame $\{\varphi_m\}_{m \in M}$ satisfies $\|\varphi_m\| = 1$ for all $m \in M$, then $\{\varphi_m\}_{m \in M}$ becomes an orthonormal basis. It immediately follows that an orthonormal basis $\{\varphi_m\}_{m \in M}$ itself is also a Parseval frame. The crucial difference between a tight frame and an orthogonal basis is that a tight frame does not need to be linearly independent, whereas an orthogonal basis is linearly independent. This means that a frame has some *redundancy*.

While the expansion of f into a Parseval frame (3) is similar to the orthonormal expansion (1), there are several ways to reconstruct f due to the redundancy. The redundancy is sometimes an obstacle from the point of view of the sparse representation of f, but the frame expansion is very useful in practice because one can calculate the coefficients by using the inner product $\langle f, \varphi_m \rangle$, as in the case of the orthogonal expansion. Furthermore, the power of redundancy in a wavelet frame yields the following:

- Wavelet frames can be much more directionally selective for image processing than standard orthogonal or biorthogonal wavelets.
- Wavelet frames can become shift invariant, whereas an orthogonal or biorthogonal wavelet transform does not become shift invariant.

- Wavelet frames are less sensitive to the erasure of coefficients, which is required for some applications such as denoising.

Based on these advantages, most multidimensional directional wavelets have redundancy and, therefore, are successfully used to analyze the directional components of multivariate functions.

4 Ridgelets

As described in the previous sections, a curvelet family is a tight frame that provides an optimal sparse approximation for the class of 2D piecewise smooth functions with C^2 singularity curves and achieves $O(M^{-2}(\log M)^3)$. Before introducing curvelets, let us introduce ridgelets [7, 8], as proposed by Candès and Donoho, which are key to the construction of first-generation curvelets.

Definition 4.1. *Let* $\gamma = (\cos\theta, \sin\theta) \in \mathbb{S}^1$ *and* $x \cdot \gamma = x_1 \cos\theta + x_2 \sin\theta$. *For each scale* $a > 0$, *each position* $b \in \mathbb{R}$, *and each orientation* $\theta \in [0, 2\pi)$, *the ridgelet transform for* $f \in L^2(\mathbb{R}^2)$ *is defined by*

$$\mathcal{RD}[f](a, b, \gamma) = \langle f, \psi_{a,b,\gamma} \rangle = \frac{1}{\sqrt{a}} \int_{\mathbb{R}^2} f(x) \overline{\psi\left(\frac{x \cdot \gamma - b}{a}\right)} \, dx,$$

where

$$\psi_{a,b,\gamma}(x) = \frac{1}{\sqrt{a}} \psi\left(\frac{x \cdot \gamma - b}{a}\right)$$

is called a ridgelet.

Remark 4.2. *A ridgelet* $\psi_{a,b,\gamma} : \mathbb{R}^2 \to \mathbb{R}$ *is oriented at angle* θ. *For a given* θ, *a ridgelet is constant along ridge lines :* $\gamma \cdot x = x_1 \cos\theta + x_2 \sin\theta$. *Transverse to these ridges is a normal wavelet* $\psi : \mathbb{R} \to \mathbb{R}$ *(see Figure 2).*

For $f \in L^1(\mathbb{R}^2) \cap L^2(\mathbb{R}^2)$, the inversion formula of the ridgelet transform is given by

$$f(x) = \frac{1}{K_{\psi,\eta}} \int_{\mathbb{S}^1} \int_{\mathbb{R}} \int_{\mathbb{R}_+} \mathcal{RD}[f](a, b, \gamma) \, \eta_{a,b,\gamma}(x) \, \frac{dadbd\gamma}{a^3},$$

if a constant $K_{\psi,\eta}$ exists:

$$K_{\psi,\eta} = \int_{\mathbb{R}^2} \frac{\hat{\psi}(\xi) \, \overline{\hat{\eta}(\xi)}}{|\xi|^2} \, d\xi < \infty,$$

where

$$\hat{f}(\xi) = \int_{\mathbb{R}^d} f(x) \, e^{-i\xi \cdot x} dx$$

is the Fourier transform of $f \in L^2(\mathbb{R}^d)$.

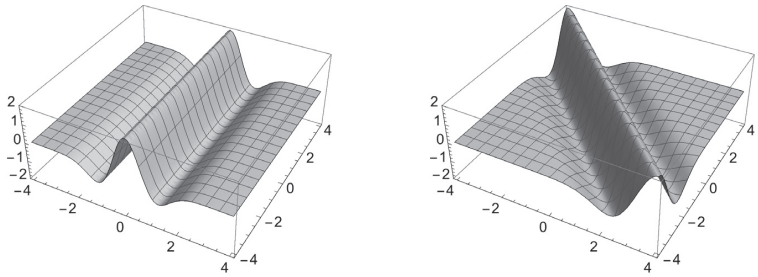

(a): $\theta = 0$ (b): $\theta = \pi/4$

Figure 2: Examples of ridgelets.

If ridgelets ψ and η are normalized such that $K_{\psi,\eta} = 1$ and $\psi = \eta$, then the Parseval relation shows that

$$\|f\|^2 = \frac{1}{4\pi} \int_{\mathbb{S}^1} \int_{\mathbb{R}} \int_{\mathbb{R}_+} |\mathcal{RD}[f](a,b,\gamma)|^2 \, \frac{dadbd\gamma}{a^3}.$$

Remark 4.3. *The ridgelet transform is essentially the combination of the 1D continuous wavelet transform and the Radon transform.*

With a wavelet $\psi_{a,b}(x) = a^{-1/2}\psi((x-b)/a)$, we define the continuous wavelet transform (CWT) $\mathcal{W}_\psi[f]$ of $f \in L^2(\mathbb{R})$ as

$$\mathcal{W}_\psi[f](a,b) = \langle f, \psi_{a,b} \rangle = \frac{1}{\sqrt{a}} \int_{\mathbb{R}} f(x) \, \overline{\psi\left(\frac{x-b}{a}\right)} \, dx.$$

The Radon transform for a bivariate function f is the collection of line integrals indexed by $(p,\theta) \in \mathbb{R} \times [0, 2\pi)$, which is given by

$$\mathcal{R}[f]\,(p,\theta) = \int_{\mathbb{R}} f\left(p\cos\theta - t\sin\theta,\, p\sin\theta + t\cos\theta\right) \, dt.$$

This can be rewritten in much simpler form using the Dirac delta function:

$$\mathcal{R}[f]\,(p,\theta) = \int_{\mathbb{R}^2} f(x)\, \delta(x_1\cos\theta + x_2\sin\theta - p)\, dx.$$

Similar to the case of ridgelets, we further rewrite the Radon transform as

$$\mathcal{R}[f]\,(p,\gamma) = \int_{\mathbb{R}^2} f(x)\, \delta(x\cdot\gamma - p)\, dx.$$

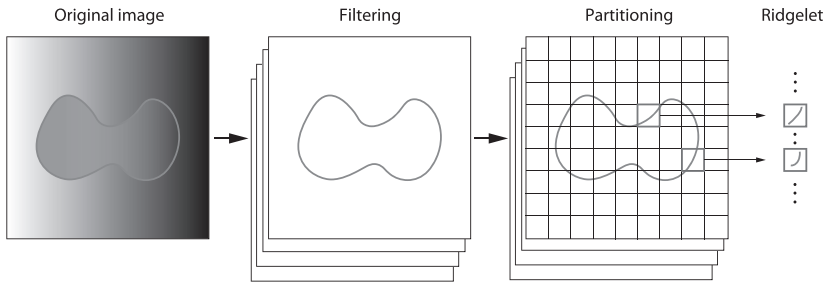

Figure 3: Key concept of the first-generation curvelet transform.

Then, we derive the relation between the CWT and the Radon transform as follows:

$$\begin{aligned}
\mathcal{RD}[f](a,b,\gamma) &= \mathcal{W}_\psi\Big[\mathcal{R}[f](p,\gamma)\Big](a,b) \\
&= \frac{1}{\sqrt{a}}\int_{\mathbb{R}}\left\{\int_{\mathbb{R}^2} f(x)\,\delta(x\cdot\gamma-p)\,dx\right\}\overline{\psi\left(\frac{p-b}{a}\right)}\,dp \\
&= \frac{1}{\sqrt{a}}\int_{\mathbb{R}^2} f(x)\left\{\int_{\mathbb{R}}\delta(x\cdot\gamma-p)\,\overline{\psi\left(\frac{p-b}{a}\right)}\,dp\right\}dx \\
&= \frac{1}{\sqrt{a}}\int_{\mathbb{R}^2} f(x)\,\overline{\psi\left(\frac{x\cdot\gamma-b}{a}\right)}\,dx = \langle f,\psi_{a,b,\gamma}\rangle.
\end{aligned}$$

5 First-Generation Curvelets

The ridgelet transform is optimal for representing straight-line singularities. Unfortunately, global straight-line singularities are rarely observed in real applications. In order to analyze local line or curve singularities, it is natural to consider part of an image and then to apply the ridgelet transform to the obtained subimages. The key concept is that edges $\approx$ ridges at very fine scale. This block, or windowed ridgelet-based transform, is referred to as the first-generation curvelet transform, which can be realized as follows:

Step 1) Multiscale filtering (subband decomposition).

Step 2) Block partitioning with a window function.

Step 3) Block ridgelet transform.

A diagram of the first-generation curvelet transform is shown in Figure 3.

Remark 5.1. *At the subband decomposition stage, a nonstandard scaling ratio, referred to as a parabolic scaling law, is used: width* $\approx$ *length*^{2}.

As described previously, this anisotropic geometric wavelet transform is an improved version of the ridgelet transform for an image that contains curve singularities. However, the first-generation curvelet transform has some drawbacks:

Block-based transform

1. The approximated curvelet images have blocking effects because the first-generation curvelet transform is a block-based transform.
2. In order to reduce the blocking effects, we need good overlapping window functions, which increases the redundancy. This dilemma must be considered as long as the block-based transform is used.

Complexity and redundancy

1. The curvelet construction is very complicated because this construction involves a seven-index structure.
2. The parabolic scaling ratio $width \approx length^2$ is not exactly true.
3. Since ridgelets are defined in polar coordinates, the implementation of the curvelet transform for discrete images on rectangular coordinates is very challenging.
4. There are many ways to implement the digital curvelet transform to solve the implementation problem, but these methods require overcomplete systems and thus are highly redundant (see [47]).

Consequently, the first-generation curvelet transform is very limited in certain applications.

6 Second-Generation Curvelets

One of the boldest decisions in developing second-generation curvelets is that they do not use ridgelets. This makes the structure of the curvelet transform substantially simpler. The construction is based on a rotation-based 2D frequency partitioning technique, holding the parabolic scaling law, $width \approx length^2$. As a result, we can expect to capture more detailed directional components of a bivariate function for finer scales compared with the standard 2D wavelet transform (see Figure 4).

We mention that multiwavelets can also realize finer frequency partitioning and have been successfully used in multidirectional analysis of images [2], but they do not have such parabolic scaling properties. The parabolic scaling allows to analyze more detailed directional components as the scale level increases, and this special anisotropic scaling law characterizes curvelets and is effective in some applications.

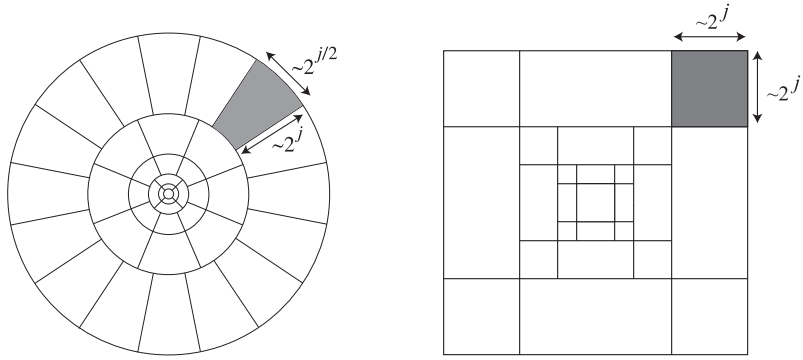

(a): Curvelet (b): Wavelet

Figure 4: 2D frequency tiling.

In this section, we shall construct the second-generation curvelets followed by [12, 37]. While there exists continuous curvelets and discrete curvelets, we only deal with the discrete curvelets that have discrete parameters for a scale, rotation and shift.

6.1 1D Orthonormal Wavelets

First, let us recall the standard 1D orthonormal wavelets. A family of wavelets is generated by a dilation and translation of a wavelet function $\psi \in L^2(\mathbb{R})$:

$$\{\psi_{j,k}(x) = 2^{j/2}\psi(2^j x - k)\}_{j,k\in\mathbb{Z}}.$$

The conditions for a wavelet $\psi \in L^2(\mathbb{R})$ such that a family of wavelets $\{\psi_{j,k}\}_{j,k\in\mathbb{Z}}$ forms an orthonormal basis of $L^2(\mathbb{R})$ are given by

$$\sum_{j\in\mathbb{Z}} |\hat{\psi}(2^j\xi)|^2 = 1, \tag{4}$$

$$\sum_{j=0}^{\infty} |\hat{\psi}(2^j\xi)|^2 \overline{\hat{\psi}(2^j(\xi + 2\pi(2m+1)))} = 0, \qquad m \in \mathbb{Z}, \tag{5}$$

which yields a typical wavelet property $\hat{\psi}(0) = \int_{\mathbb{R}} \psi(x)\, dx = 0$.

Condition (4) is that for a Parseval frame and is called the *partition of unity*, whereas (5) ensures the orthogonality of a frame. The curvelet construction begins by focusing on the partition of unity (4) in $\mathbb{R}^2$ while giving up the orthogonality (5). In the case of one dimension, the partition of unity (4) means that dyadic dilation of one fixed function $\hat{\psi}$ gives a tiling of the frequency domain $\mathbb{R}\backslash\{0\}$. However, this tiling is not unique for two dimensions, because the plane $\mathbb{R}^2$ has a directional degree of freedom.

6.2 Window Functions

Let us now consider the 2D version of the partition of unity with window functions in the frequency domain represented by polar coordinates (r, ω), where $r = |\xi| = \sqrt{\xi_1^2 + \xi_2^2}$ and $\omega = \arctan \xi_2/\xi_1$. We introduce a pair of smooth, nonnegative, real-valued C^∞ window functions, namely, a radial window $W(r)$ for a scale j, and an angular window $V(t)$ for an angle ω. The support of these functions are supp $W \subset (1/2, 2)$ and supp $V \subset [-1, 1]$. Both windows satisfy the following conditions, which are referred to as the *admissibility conditions*:

$$\sum_{j \in \mathbb{Z}} |W(2^{-j} r)|^2 = 1, \qquad r > 0, \tag{6}$$

$$\sum_{\ell \in \mathbb{Z}} |V(t - \ell)|^2 = 1, \qquad t \in \mathbb{R}. \tag{7}$$

Definition 6.1. *For $r \geq 0$ and $\omega \in [0, 2\pi)$, a wedge window $U_j(r, \omega)$, $j \geq 0$ is defined in the frequency domain as*

$$U_j(r, \omega) = 2^{-3j/4} W(2^{-j} r)\, V\left(\frac{N_j\, \omega}{2\pi}\right),$$

where $N_j = 4 \cdot 2^{\lfloor j/2 \rfloor}$ is the number of wedges at each scale j and $\lfloor x \rfloor$ is the integer part of x.

A wedge window U_j is localized in a polar wedge, and its support is defined as the support of W and V. Note that several different definitions of U_j can be found in the literature. For examples, the ceiling function $\lceil x \rceil = \min\{n \in \mathbb{Z} \mid n \geq x\}$ is used in stead of the floor function $\lfloor x \rfloor = \max\{n \in \mathbb{Z} \mid n \leq x\}$.

Definition 6.2. *We define a basic (mother) curvelet as $\hat{\phi}_{j,0,0}(\xi) = U_j(\xi)$. With its inverse Fourier transform, a family of curvelets are generated by a collection of waveforms $\phi_{j,k,\ell} \in L^2(\mathbb{R}^2)$ defined as*

$$\phi_{j,k,\ell}(x) = \phi_{j,0,0}\left(R_{\theta_{j,\ell}}\left(x - x_k^{(j,\ell)}\right)\right),$$

where

- *R_θ is the clockwise rotation matrix by θ, and $R_{-\theta} = R_\theta^T$ is the anticlockwise one.*
- *$x_k^{(j,\ell)} = R_{-\theta_{j,\ell}}\left(k_1\, 2^{-j},\, k_2\, 2^{-j/2}\right)$ is a shift parameter with parabolic scaling.*
- *$\theta_{j,\ell} = 2^{-\lfloor j/2 \rfloor}\, \ell\, \pi/2$ for $0 \leq \ell < N_j$ is the equidistant sequence of rotation angles.*

Remark 6.3. *In this definition of curvelets, $\phi_{j,k,\ell}$ becomes a complex-valued function. One can obtain real-valued curvelets by $U_j(r, \theta) + U_j(r, \theta + \pi)$.*

The discrete curvelet transform is simply written as the inner product between a function $f \in L^2(\mathbb{R}^2)$ and a curvelet element $\phi_{j,k,\ell}$:

$$c_{j,k,\ell} = \langle f, \phi_{j,k,\ell} \rangle = \int_{\mathbb{R}^2} f(x)\, \overline{\phi_{j,k,\ell}(x)}\, dx,$$

where the sequence $\{c_{j,k,\ell} \mid j \geq 0,\, k \in \mathbb{Z}^2,\, 0 \leq \ell \leq N_j\}$ is called the curvelet coefficient. In general, the curvelet transform is implemented in the frequency domain. When the Parseval's identity is applied to the above inner product, it is convenient to write the curvelet transform in the frequency domain as

$$\begin{aligned}
\langle f, \phi_{j,k,\ell} \rangle &= \int_{\mathbb{R}^2} f(x)\, \overline{\phi_{j,k,\ell}(x)}\, dx \\
&= \frac{1}{(2\pi)^2} \int_{\mathbb{R}^2} \hat{f}(\xi)\, \overline{\hat{\phi}_{j,k,\ell}(\xi)}\, d\xi \\
&= \frac{1}{(2\pi)^2} \int_{\mathbb{R}^2} \hat{f}(\xi)\, \hat{\phi}_{j,0,0}(R_{\theta_{j,\ell}}\, \xi)\, e^{i\xi \cdot x_k^{(j,\ell)}}\, d\xi \\
&= \frac{1}{(2\pi)^2} \int_{\mathbb{R}^2} \hat{f}(\xi)\, U_j(R_{\theta_{j,\ell}}\, \xi)\, e^{i\xi \cdot x_k^{(j,\ell)}}\, d\xi.
\end{aligned}$$

6.3 Partition of Unity

For such window functions that satisfy the admissibility conditions (6) and (7), we present the following example.

Example 6.4. *In [37], the Meyer type window functions are introduced, which are defined by*

$$W(r) = \begin{cases} \cos\left[\frac{\pi}{2}\nu\,(5-6r)\right], & 2/3 \leq r \leq 5/6, \\ 1, & 5/6 \leq r \leq 4/3, \\ \cos\left[\frac{\pi}{2}\nu\,(3r-4)\right], & 4/3 \leq r \leq 5/3, \\ 0, & \textit{otherwise}, \end{cases}$$

and

$$V(t) = \begin{cases} 1, & |t| \leq 1/3, \\ \cos\left[\frac{\pi}{2}\nu\,(3|t|-1)\right], & 1/3 \leq |t| \leq 2/3, \\ 0, & \textit{otherwise}, \end{cases}$$

where ν is a smooth function such that

$$\nu(x) = \begin{cases} 0, & x \leq 0, \\ 1, & x \geq 1, \end{cases} \quad \textit{and} \quad \nu(x) + \nu(1-x) = 1.$$

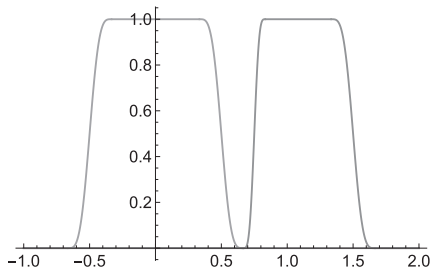

Figure 5: Example of window functions $W(r)$ and $V(t)$.

The smoothness of the wedge window U_j depends on the smoothness of both radial and angular windows W and V. One can design the smoothness by using polynomials for ν. Figure 5 shows the above window functions W and V. Here, we set ν as a third-order polynomial: $\nu(x) = 3x^2 - 2x^3$.

With these window functions, we have the following observation for the 2D partition of unity [37].

Proposition 6.5. *Let $D = \{r\,(\cos\omega, \sin\omega) \in \mathbb{R}^2 \mid 0 \le r \le 1,\, 0 \le \omega < 2\pi)\}$ be a closed unit disc. A set of polar wedges U_j covers the frequency plane $\mathbb{R}^2\backslash\{D\}$ as*

$$\sum_{j\ge 0} \sum_{0\le \ell < N_j} 2^{3j/2} \left| U_j\left(r, \omega - \frac{2\pi\ell}{N_j}\right)\right|^2 = 1.$$

Proof. According to the admissibility condition (7), for the tiling of a circular ring by the wedge windows U_j, we need 2π-periodizations of the angular window V that satisfies, for all $\omega \in [0, 2\pi)$,

$$\sum_{0\le \ell < N_j} \left| V\left(\frac{N_j}{2\pi}\left\{\omega - \frac{2\pi\ell}{N_j}\right\}\right)\right|^2 = \sum_{0\le \ell < N_j} \left| V\left(\frac{N_j}{2\pi}\omega - \ell\right)\right|^2 = 1.$$

Note that the case $\ell = 0 = N_j$ yields the same result due to the periodicity.

Substituting it to the sum of U_j with respect to all scales $2^{-j}, j \ge 0$ and all numbers of rotation $0 \le \ell < N_j$, we have

$$\begin{aligned}
\sum_{j\ge 0} \sum_{0\le \ell < N_j} 2^{3j/2} \left| U_j\left(r, \omega - \frac{2\pi\ell}{N_j}\right)\right|^2 &= \sum_{j\ge 0} \sum_{0\le \ell < N_j} \left| W(2^{-j}r)\, V\left(\frac{N_j}{2\pi}\omega - \ell\right)\right|^2 \\
&= \sum_{j\ge 0} \left|W(2^{-j}r)\right|^2 \sum_{0\le \ell < N_j} \left| V\left(\frac{N_j}{2\pi}\omega - \ell\right)\right|^2 \\
&= \sum_{j\ge 0} \left|W(2^{-j}r)\right|^2 .
\end{aligned}$$

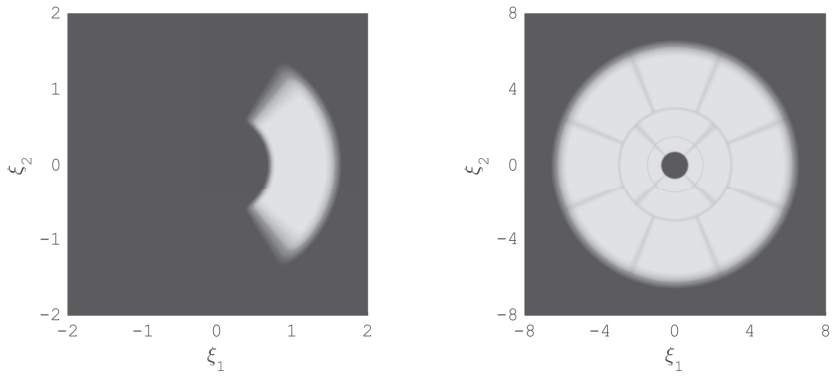

(a) (b)

Figure 6: Examples of curvelets. (a): $\hat{\phi}_{0,0,0}(\xi)$. (b): $\sum_{0\le j\le 2}\sum_{0\le \ell<N_j} 2^{3j/2}\left|\hat{\phi}_{j,k,\ell}(\xi)\right|^2$.

Thus, with the admissibility condition for the radial window (6) and supp $W \subset (1/2, 2)$, it holds that, for $r > 1$,

$$\sum_{j\ge 0}\left|W(2^{-j}r)\right|^2 = 1.$$

□

Remark 6.6. *For complete coverage of the frequency plane, we need a low-pass window function $W_0(r)$ such that*

$$|W_0(r)|^2 + \sum_{j\ge 0}|W(2^{-j}r)|^2 = 1.$$

Proposition 6.5 implies that the partition of unity (4) for the curvelet family $\{\phi_{j,k,\ell} \mid 0 \le j < \infty,\, k \in \mathbb{Z}^2,\, 0 \le \ell < N_j\}$ becomes

$$\sum_{j\ge 0}\sum_{0\le \ell<N_j} 2^{3j/2}|\hat{\phi}_{j,k,\ell}(\xi)|^2 = 1, \qquad |\xi| > 1, \tag{8}$$

where $\xi = r\,(\cos\omega, \sin\omega)$ and

$$\hat{\phi}_{j,\ell,k}(\xi) = U_j\left(r, \omega - \frac{2\pi\ell}{N_j}\right) e^{-i\xi\cdot x_k^{(j,\ell)}} = 2^{-3j/4} W(2^{-j}r)\, V\left(\frac{N_j}{2\pi}\omega - \ell\right) e^{-i\xi\cdot x_k^{(j,\ell)}}.$$

Figure 6(a) shows a picture of the basic curvelet $\hat{\phi}_{0,0,0}(\xi)$ constructed by choosing the window functions W and V given in Example 6.4. We illustrate the partition of unity (8) for $0 \le j \le 2$ in Figure 6(b), which demonstrates how the collection of curvelet elements tiles the entire frequency plane $\mathbb{R}^2$.

Theorem 6.7 (Candés and Donoho [12], Theorem 4.2). *Let* $\{\phi_{j,k,\ell}\}_{j,k,\ell}$ *be a curvelet family. For all* $f \in L^2(\mathbb{R}^2)$ *that satisfy* $\hat{f}(\xi) = 0$ $(|\xi| < 1)$,

$$f = \sum_{j\geq 0} \sum_{k\in\mathbb{Z}^2} \sum_{0\leq \ell < N_j} \langle f, \phi_{j,k,\ell}\rangle \, \phi_{j,k,\ell}, \tag{9}$$

and

$$\|f\|^2 = \sum_{j\geq 0} \sum_{k\in\mathbb{Z}^2} \sum_{0\leq \ell < N_j} |\langle f, \phi_{j,k,\ell}\rangle|^2 . \tag{10}$$

The proof can be found in [11].

We can construct a coarse (*father*) curvelet for a low-pass window function as

$$\hat{\phi}_{j_0}(\xi) = 2^{-j_0} W_{j_0}(2^{-j_0}|\xi|), \qquad \phi_{j_0,k}(x) = \phi_{j_0}(x - 2^{-j_0}k),$$

where W_{j_0}, $j_0 \geq 0$ is a coarse radial window function such that

$$|W_{j_0}(r)|^2 + \sum_{j\geq j_0} |W(2^{-j}r)|^2 = 1. \tag{11}$$

The coarse curvelet ϕ_{j_0} is a nondirectional element of the curvelet family. Such a function that satisfies (11) is a 2D Meyer type scaling function.

With the "full family" of curvelets,

$$\{\phi_{j_0,k} \mid j_0 \geq 0,\, k \in \mathbb{Z}^2\} \cup \{\phi_{j,k,\ell} \mid j_0 \leq j < \infty,\, k \in \mathbb{Z}^2,\, 0 \leq \ell < N_j\},$$

the reconstruction formula (9) and the Parseval relation (10) for all $f \in L^2(\mathbb{R}^2)$ may be be formulated as follows:

$$f = \sum_{j\geq j_0} \sum_{k\in\mathbb{Z}^2} \sum_{0\leq \ell < N_j} \langle f, \phi_{j,k,\ell}\rangle \, \phi_{j,k,\ell} + \sum_{k\in\mathbb{Z}^2} \langle f, \phi_{j_0,k}\rangle \, \phi_{j_0,k},$$

and

$$\|f\|^2 = \sum_{j\geq j_0} \sum_{k\in\mathbb{Z}^2} \sum_{0\leq \ell < N_j} |\langle f, \phi_{j,k,\ell}\rangle|^2 + \sum_{k\in\mathbb{Z}^2} |\langle f, \phi_{j_0,k}\rangle|^2 .$$

6.4 Properties of Second-Generation Curvelets

We summarize important properties of second-generation curvelets as follows:

- **Tight frame:** Theorem 6.7 implies that a family of curvelets $\{\phi_{j,k,\ell}\}_{j,k,\ell}$ generates a Parseval frame of $L^2(\mathbb{R}^2)$, which guarantees the exact reconstruction of $f \in L^2(\mathbb{R}^2)$ from the curvelet coefficients $\langle f,\, \phi_{j,k,\ell}\rangle$ as in (9), and it provides energy preservation $\|f\|^2 = \|c_{j,k,\ell}\|^2$ as in (10).

- **Support:** The curvelet $\hat{\phi}_{j,k,\ell}$ has compact support because it is localized on the wedge in the frequency domain. As a result, $\phi_{j,k,\ell}$ cannot has compact support and thus is an infinitely oscillating function. According to support of the window functions W and V, the curvelet $\hat{\phi}_{j,k,\ell}$ is supported inside the polar wedge with

$$2^{j-1} \leq r \leq 2^{j+1}, \quad \text{and} \quad -\frac{2^{-\lfloor j/2 \rfloor}\pi(-1-\ell)}{2} \leq \omega \leq \frac{2^{-\lfloor j/2 \rfloor}\pi(-1-\ell)}{2},$$

  which implies that support of curvelets is based on the parabolic scaling ratio described below.

- **Parabolic scaling:** Based on Definition 6.2, the curvelet $\phi_{j,k,\ell}$ has the anisotropy scaling relation

$$width \approx 2^{-j}, \quad length \approx 2^{-j/2} \;\Rightarrow\; width \approx length^2.$$

  In the frequency domain, this relation becomes $width \approx 2^j$ and $length \approx 2^{j/2}$. This makes curvelets very long and needle-shaped in a radial direction at a very fine scale. Thus, the shape of a localized wedge window U_j is similar to a brush, especially at a very fine scale. As such, it is natural to refer to these windows as brushlets or wedgelets, rather than curvelets, although both names have been proposed already in [40, 22].

- **Vanishing moments:** Due to the anisotropy localization on the frequency plane, the curvelet has anisotropic oscillatory behavior. For example, $\phi_{0,0,0}(x)$ is more oscillatory in the x_1 direction than in the x_2 direction. Thus, for all x_2, the curvelet $\phi_{0,0,0}(x)$ has p vanishing moments such that

$$\int_{\mathbb{R}} \phi_{0,0,0}(x_1, x_2)\, x_1^n \, dx_1 = 0, \qquad 0 \leq n < p.$$

  The same property also holds for rotated or shifted curvelets to which correct coordinates are taken.

6.5 Digital Curvelets

From the point of view of applications, there is still a problem with second-generation curvelets. Working in polar coordinates makes the curvelet construction very simple and elegant in the continuous domain, but causes an implementation problem for handling discrete images that are, in general, sampled on a rectangular grid.

The digital curvelet transform is thus considered to solve this problem. The idea is to use shearing on the Cartesian coordinates, instead of rotation on the polar coordinates.

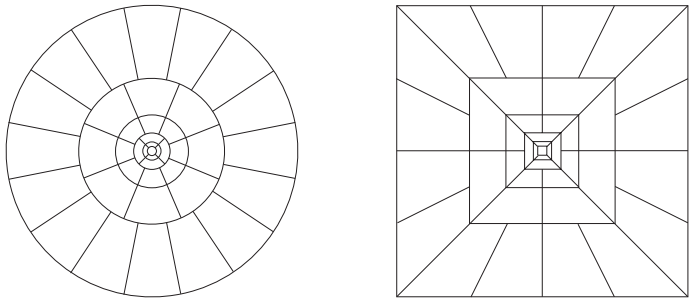

(a) (b)

Figure 7: 2D frequency tiling. (a): Polar grid for the continuous domain. (b): Pseudo-polar grid for the discrete domain.

This also provides an exact tiling of the frequency plane $\mathbb{R}^2$ based on concentric squares with the parabolic scaling law (see Figure 7).

Suppose that $\hat{\phi}^D_{j,0,0}(\xi)$ is a Cartesian wedge that is localized on the region of the tiling. Then, curvelets on the Cartesian coordinates are given by

$$\phi^D_{j,k,\ell}(x) = \phi^D_{j,0,0}\left(S_{\tilde{\theta}_{j,\ell}}\left(x - \tilde{x}^{(j,\ell)}_k\right)\right),$$

where $S_{\tilde{\theta}_{j,\ell}}$ is a shear matrix

$$S_{\tilde{\theta}_{j,\ell}} = \begin{pmatrix} 1 & -\tan\tilde{\theta}_{j,\ell} \\ 0 & 1 \end{pmatrix},$$

for equispaced slopes $\tilde{\theta}_{j,\ell}$, and $\tilde{x}^{(j,k)}_k = S^{-1}_{\tilde{\theta}_{j,\ell}}(k_1\, 2^{-j}, k_2\, 2^{-\lfloor j/2 \rfloor})$ represents the position of $\phi^D_{j,k,\ell}$. The curvelet coefficients are then computed by

$$c^D_{j,k,\ell} = \langle f, \phi^D_{j,k,\ell}\rangle = \int_{\mathbb{R}^2} f(x)\,\overline{\phi^D_{j,k,\ell}(x)}\,dx = \frac{1}{(2\pi)^2}\int_{\mathbb{R}^2} \hat{f}(\xi)\,\overline{\hat{\phi}^D_{j,k,\ell}(\xi)}\,d\xi.$$

While this discrete curvelet transform is the redundant transform, there is a fast computation algorithm available that achieves $O(N^2 \log N)$ for a digital image $f \in \mathbb{R}^{N\times N}$[15]. Codes are available from CurveLab (`http://curvelab.org`).

6.6 Applications of Curvelets

Curvelets have a wide range of applications, not limited to image processing. The first-generation curvelet transform was applied for the first time to image denoising [47, 16] and was then extended to other image processing tasks such as image contrast enhancement [50] and astronomical image representation [48, 18].

The second-generation curvelet transform has also been successfully applied and shown to be a very efficient tool for many applications in image processing, including the 3D case, such as denoising [36, 44, 53], motion estimation and video tracking of geophysical flows [33], morphological component analysis [5, 49], watermarking [55], deblurring [32], and inpainting [28]. The applications of curvelets have been further extended to other scientific fields, such as seismic data exploration [27, 23, 17], turbulent analysis in fluid mechanics [4, 34, 35], solving partial differential equations (PDEs) [52], compressed sensing [45], and reconstruction problem of tomography [25]. For details on each application, see [37].

7 Other Multidirectional Methods

In the remainder of this paper, we briefly note two multiscale multidirectional methods similar to curvelets, namely, shearlets [31] and contourlets [21], both of which are tight frames of $L^2(\mathbb{R}^2)$.

7.1 Shearlets

After the proposal of curvelets, the shearlet, the concept of which is very similar to second-generation curvelets, was proposed. Shearlets are generated by scaling, shear, and translation of a basic (mother) shearlet function. The shear operation is key because this operation captures the direction of singularities of an image. Therefore, the discretized second-generation curvelet transform is very similar to the shearlet transform.

Let $A_a = \begin{pmatrix} a & 0 \\ 0 & \sqrt{a} \end{pmatrix}$, $a > 0$ be a dilation matrix, and let $S_s = \begin{pmatrix} 1 & s \\ 0 & 1 \end{pmatrix}$, $s \in \mathbb{R}$ be a shearing matrix. The shearlets $\psi_{a,s,k}$ is then defined as

$$\psi_{a,s,k}(x) = a^{-3/4}\,\psi\left(A_a^{-1}\,S_s^{-1}\,(x-k)\right) = a^{-3/4}\,\psi\left(\begin{pmatrix} 1/a & -s/a \\ 0 & 1/\sqrt{a} \end{pmatrix}(x-k)\right),$$

where a shearlet function $\psi \in L^2(\mathbb{R}^2)$ is designed in the Fourier domain using the 2D partition of unity with a dilated shearing operation. The shearlet transform $\mathcal{SH}[f]$ of $f \in L^2(\mathbb{R}^2)$ is defined as

$$\mathcal{SH}[f](a,s,k) = \langle f, \psi_{a,s,k} \rangle.$$

Although this is a continuous integral transform, fast and discrete algorithms are also available (see [26]).

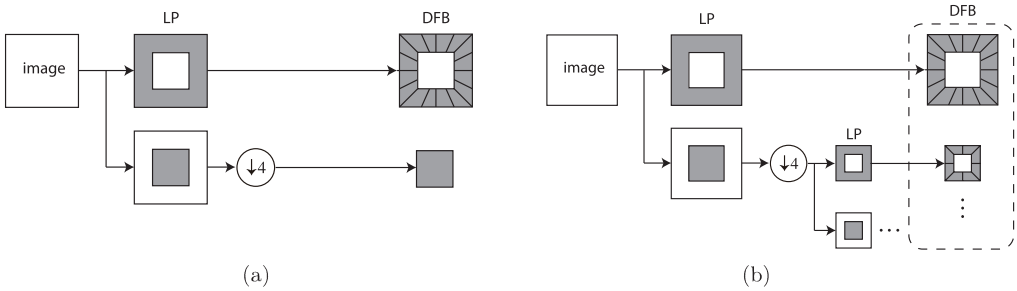

Figure 8: The contourlet transform. (a): one iteration. (b): two iterations.

7.2 Contourlets

A contourlet is based on a discrete setting design. The contourlet is a purely discrete filter bank version of the curvelet framework. In the construction of contourlets, we need only classical signal processing operators, such as convolution (filtering) and subsampling. A double-iterated filter bank structure, called the contourlet filter bank, plays a central role in the contourlet framework, which consists of two stages, the Laplacian pyramid (LP) [6] and the directional filter bank (DFB) as follows:

Stage 1) In the LP stage, a 2D signal is decomposed into low-pass and high-pass components, whereas the low-pass component is then subsampled by a factor of 2 for each direction x_1 and x_2.

Stage 2) In the next DFB stage, sharing is first applied to the high-pass component transformed by the LP. A fan filter is then applied it to obtain horizontally and vertically filtered signals. Finally, quincunx sampling, which performs discrete rotation with angle $\pi/4$ and subsampling by a factor of 2, is applied for each direction x_1 and x_2.

A sequence of these operations can be iterated until an arbitrary decomposition level by setting the low-pass component as a new input signal. Figure 8 illustrates the diagram of the contourlet transform.

The contourlet transform has the following properties:

- If both the LP and the DFB use perfect reconstruction filters, then the discrete contourlet transform provides a frame of $\ell^2(\mathbb{Z}^2)$.

- If the filters are orthonormal filters, then the frame becomes a Parseval frame.

- Since the DFB is critically sampled, the total redundancy of the contourlet transform up to a scale level of J is less than $4/3$: $1 + \sum_{j=1}^{J} (1/4)^j < 4/3$.

- Let $l_j, j = 0, 1, \ldots$ be a level of DFB at each pyramidal level j of the LP. Basis images of the contourlet transform have a support size of parabolic scaling ratio $width \approx C\, 2^j$ and $length \approx C\, 2^{j+l_j-2}$.

We finish this paper by pointing out the importance and influence that the contourlets have on other multiscale multidirectional wavelets, such as curvelets and shearlets. Although the filter-bank-based discrete approach of contourlets for constructing a curvelet-like framework has an advantage in that a discrete setting provides fast and easy implementations, a proper continuum theory is missing and its formulation is rather complicated. However, we note that contourlets are important for the following two reasons:

- **Discrete parabolic scaling:** Discrete squared frequency partitioning with the parabolic scaling law was perhaps first introduced in the contourlet transform. A similar structure was later used in second-generation curvelets and shearlets.

- **Shearing:** A shearing-based method in DFB to obtain directional components was also used in second-generation curvelets and shearlets.

Acknowledgments

The author would like to thank Tamotu Kinoshita and Katsuya Fujii for various useful comments which significantly improved the presentation of this paper. This work was partially supported by JSPS KAKENHI Grant Number 17K12716.

References

[1] J. Antoine, P. Carrette, R. Murenzi, and B. Piette, Image analysis with two-dimensional continuous wavelet transform, Signal Process., **31** (1993), 241–272.

[2] R. Ashino, S. Desjardins, C. Heil, M. Nagase and R. Vaillancourt, Smooth tight frame wavelets and image microanalysis in the Fourier domain, Comput. Math. Appl., **45** (2003), 1551–1579.

[3] R. Bamberger and M. Smith, A filter bank for the directional decomposition of images: theory and design, IEEE Trans. Signal Process., **40** (1992), 882–893.

[4] I. Bermejo-Moreno and D. Pullin, On the non-local geometry of turbulence, J. Fluid Mech., **603** (2008), 101–135.

[5] J. Bobin, J. Starck, J. Fadili, Y. Moudden, and D. Donoho, Morphological component analysis: an adaptive thresholding strategy, IEEE Trans. Image Process., **16** (2007), 2675–2681.

[6] P. Burt and E. Adelson, The Laplacian pyramid as a compact image code, IEEE Trans. Commun., **31** (1983), 532–540.

[7] E. Candès, Harmonic analysis of neural networks, Appl. Comput. Harmon. Anal., **6** (1999), 197–218.

[8] E. Candès and D. Donoho, Ridgelets: a key to higher-dimensional intermittency?, Philos. Trans. R. Soc. London A, Math. Phys. Eng. Sci., **357** (1999), 2495–2509.

[9] E. Candès and D. Donoho, Curvelets – A surprisingly effective nonadaptive representation for objects with edges, in Curves and Surface Fitting: Saint-Malo 1999, A. Cohen, C. Rabut, and L. Schumaker, Eds. Nashville: Vanderbilt Univ. Press, 105–120, 2000.

[10] E. Candès and D. Donoho, New tight frames of curvelets and optimal representations of objects with piecewise C^2 singularities, Comm. Pure and Appl. Math., **56** (2004), 216–266.

[11] E. Candès and D. Donoho, Continuous curvelet transform. I. Resolution of the wavefront set, Appl. Comput. Harmon. Anal., **19** (2005), 162–197.

[12] E. Candès and D. Donoho, Continuous curvelet transform. II. Discretization and frames, Appl. Comput. Harmon. Anal., **19** (2005), 198–222.

[13] E. Candès and L. Demanet, Curvelets and Fourier integral operators, C. R. Math. Acad. Sci. Paris, **336** (2003), 395–398.

[14] E. Candès and L. Demanet, The curvelet representation of wave propagators is optimally sparse, Comm. Pure Appl. Math., **58** (2005), 1472–1528.

[15] E. Candès, L. Demanet, D. Donoho, and L. Ying, Fast discrete curvelet transforms, Multiscale Model. Simul., **5** (2006), 861–899.

[16] E. Candès and F. Guo, New multiscale transforms, minimum total variation synthesis: applications to edge-preserving image reconstruction, Signal Process., **82** (2002), 1519–1543.

[17] H. Chauris and T. Nguyen, Seismic demigration/migration in the curvelet domain, Geophysics, **73** (2008), S35–S46.

[18] M. Choi, R. Kim, M. Nam, and H. Kim, Fusion of multispectral and panchromatic satellite images using the curvelet transform, IEEE Geosci. Remote Sens. Lett., **2** (2005), 136–140.

[19] I. Daubechies, Ten Lectures on Wavelets, CBMS-NSF Regional Conf. Series in Appl. Math., SIAM, Philadelphia, 1992.

[20] I. Daubechies, B. Han, A. Ron, and Z. Shen, Framelets: MRA-based constructions of wavelet frames, Appl. Comput. Harmon. Anal., **14** (2003), 1–46.

[21] M. Do and M. Vetterli, The contourlet transform: an efficient directional multiresolution image representation, IEEE Trans. Image Process., **14** (2005), 2091–2106.

[22] D. Donoho, Wedgelets: nearly minimax estimation of edges, Ann. Statist., **27** (1999), 859–897.

[23] H. Douma and M. Hoop, Leading-order seismic imaging using curvelets, Geophysics, **72** (2007), S231–S248.

[24] R. Duffin and A. Schaeffer, A class of nonharmonic Fourier series, Trans. Amer. Math. Soc., **72** (1952), 341–366.

[25] J. Frikel, Sparse regularization in limited angle tomography, Appl. Comput. Harmon. Anal., **34** (2013), 117–141.

[26] S. Häuser and G. Steidl, Fast finite shearlet transform: a tutorial, arXiv:1202.1773v2, (2014).

[27] G. Hennenfent and F. Herrmann, Seismic denoising with nonuniformly sampled curvelets, Comput. Sci. Eng., **8** (2006), 16–25.

[28] L. Jiang, X. Feng, and H. Yin, Structure and texture image inpainting using sparse representations and an iterative curvelet thresholding approach, Int. J. Wavelets Multiresolut. Inf. Process., **6** (2008), 691–705.

[29] N. Kingsbury, Complex wavelets for shift invariant analysis and filtering of signals, Appl. Comput. Harmon. Anal., **10** (2001), 234–253.

[30] J. Kovačević and M. Vetterli, Nonseparable multidimensional perfect reconstruction filter banks and wavelet bases for $\mathbb{R}^n$, IEEE Trans. Inform. Theory, **38** (1992), 533–555.

[31] D. Labate, W. Lim, G. Kutyniok, and G. Weiss, Sparse multidimensional representation using shearlets, in Wavelets XI, edited by M. Papadakis, A. F. Laine, and M. A. Unser, SPIE Proc. 5914 (2005), SPIE, Bellingham, WA, 254–262, 2005.

[32] J. Ma, Deblurring using singular integrals and curvelet shrinkage, Phys. Lett. A, **368** (2007), 245–250.

[33] J. Ma, A. Antoniadis, and F. Dimet, Curvelet-based multiscale detection and tracking for geophysical fluids, IEEE Trans. Geosci. Remote Sensing, **44** (2006), 3626–3637.

[34] J. Ma and M. Hussaini, Three-dimensional curvelets for coherent vortex analysis of turbulence, Appl. Phys. Lett., **91** (2007), 184101:1–184101:3.

[35] J. Ma, M. Hussaini, O. Vasilyev, and F. Dimet, Multiscale geometric analysis of turbulence by curvelets, Phys. Fluids, **21** (2009), 075104.

[36] J. Ma and G. Plonka, Combined curvelet shrinkage and nonlinear anisotropic diffusion, IEEE Trans. Image Process., **16** (2007), 2198–2206.

[37] J. Ma and G. Plonka, The curvelet transform, IEEE Signal Processing Magazine, **27** (2010), 118–133.

[38] S. Mallat, A Wavelet Tour of Signal Processing, 3rd ed., Academic Press, 2008.

[39] S. Mallat, Geometrical grouplets, Appl. Comput. Harmon. Anal., **26** (2009), 161–180.

[40] F. Meyer and R. Coifman, Brushlets: a tool for directional image analysis and image compression, Appl. Comput. Harmon. Anal., **4** (1997), 147–187.

[41] B. Olshausen and D. Field, Emergence of simple-cell receptive field properties by learning a sparse code for natural images, Nature **381** (1996), 607–609.

[42] E. Pennec and S. Mallat, Image compression with geometric wavelets. In Proc. IEEE Int. Conf. on Image Proc., Vancouver, Canada, Sep. 2000.

[43] E. Pennec and S. Mallat, Sparse geometrical image approximation with bandlets, IEEE Trans. Image Process., **14** (2005), 423–438

[44] G. Plonka and J. Ma, Nonlinear regularized reaction-diffusion filters for denoising of images with textures, IEEE Trans. Image Process., **17** (2008), 1283–1294.

[45] G. Plonka and J. Ma, Curvelet-wavelet regularized split Bregman method for compressed sensing, Int. J. Wavelets Multiresolut. Inf. Process., **9** (2011), 79–110.

[46] E. Simoncelli, W. Freeman, E. Adelson, and D. Heeger, Shiftable multiscale transforms, IEEE Trans. Inform. Theory, **38** (1992), 587–607.

[47] J. Starck, E. Candès, and D. Donoho, The curvelet transform for image denoising, IEEE Trans. Image Process., **11** (2002), 670–684.

[48] J. Starck, E. Candès, and D. Donoho, Astronomical image representation by the curvelet transform, Astron. Astrophys., **398** (2003), 785–800.

[49] J. Starck, M. Elad, and D. Donoho, Image decomposition via the combination of sparse representation and a variational approach, IEEE Trans. Image Process., **14** (2005), 1570–1582.

[50] J. Starck, F. Murtagh, E. Candès, and D. Donoho, Gray and color image contrast enhancement by the curvelet transform, IEEE Trans. Image Process., **12** (2003), 706–717.

[51] G. Strang and T. Nguyen, Wavelets and Filter Banks, Wellesley-Cambridge Press, 1996.

[52] B. Sun, J. Ma, H. Chauris, and H. Yang, Solving the wave equation in the curvelet domain: a multiscale and multidirectional approach, J. Seismic Exploration, **18** (2009), 385–399.

[53] L. Tessens, A. Pizurica, A. Alecu, A. Munteanu, and W. Philips, Context adaptive image denoising through modeling of curvelet domain statistics, J. Electron. Imaging, **17** (2008), 03021:1–03021:17.

[54] V. Velisavljevic, B. Beferull-Lozano, M. Vetterli, and P. Dragotti, Directionlets: anisotropic multidirectional representation with separable filtering, IEEE Trans. Image Process., **15** (2006), 1916–1933.

[55] C. Zhang, L. Cheng, Z. Qiu, and L. Cheng, Multipurpose watermarking based on multiscale curvelet transform, IEEE Trans. Inform. Forensics Security, **3** (2008), 611–619.

Department of Mathematical Sciences
Tokai University
Kanagawa 259-1292
JAPAN
E-mail address: `fujinoki@tokai-u.ac.jp`

東海大学・理学部情報数理学科　藤ノ木健介